Negative spin polarization and effect of composition on the atomic order and electronic structure of Mn_2VAl Heusler alloy thin films

Hirofumi Suto[1*], Vineet Barwal[1], Keisuke Masuda[1], Kodchakorn Simalaotao[1], Taisuke Sasaki[1], Yoshio Miura[1], Hiroo Tajiri[2], Loku Singgappulige Rosantha Kumara[2], Tomoyuki Koganezawa[2], and Yuya Sakuraba[1]

[1]Research Center for Magnetic and Spintronic Materials, National Institute for Materials Science (NIMS), Tsukuba, 305-0047, Japan

[2]Japan Synchrotron Radiation Research Institute (JASRI), Kouto, 679-5198, Japan

[*]SUTO.Hirofumi@nims.go.jp

Abstract

We explored Mn_2VAl (MVA) Heusler alloy thin films to investigate their potential as a material with negative spin polarization. Density-of-state calculations showed that MVA has a gap in the majority-spin state at the Fermi energy, leading to negative spin polarization. Negative spin polarization was found to be higher in the $L2_1$-ordered state than that in the $B2$-ordered state. V_{Mn} antisites (V atoms occupying Mn sites) introduced an in-gap state that significantly reduced negative spin polarization, while Mn_V and Al_V antisites preserved the energy gap and thus weakly affected negative spin polarization. High-quality MVA films were fabricated via magnetron sputtering at elevated temperatures, achieving the $B2$ and $L2_1$ order parameters of 0.88 and 0.5 at 600°C in the stoichiometric composition, respectively. The comparison of stoichiometric and various off-stoichiometric samples revealed that the Mn-rich and Al-rich compositions showed an improved ordering and a smaller number of V_{Mn} antisites. The benefit of using off-stoichiometric compositions was further highlighted by the obtained negative magnetoresistance, which was measured via epitaxial MVA/Ag spacer/CoFe current-perpendicular-to-plane giant magnetoresistance devices. Devices with the MVA composition of $Mn_{2.2}V_{0.6}Al_{1.2}$ showed a very large negative magnetoresistance of −4.4%, indicating high negative spin polarization in MVA. Furthermore, highly efficient spin-transfer torque generation, with a torque direction opposite to that seen in positive spin polarization materials, was demonstrated via spin injection from MVA.

I. Introduction

Co-based Heusler alloys have been studied extensively for the use in various spintronic applications [1–7] due to their predicted high spin polarization (P) and high Curie temperature. Furthermore, large magnetoresistance (MR) and high spin-transfer torque (STT) efficiency have been experimentally demonstrated in these materials [8–15]. Contrary to Co-based alloys, Mn-based Heusler alloys have not been as extensively studied despite the theoretical predictions of high P and large perpendicular magnetic anisotropy in them [16,17,26–32,18–25]. Therefore, this study focuses on a Mn-based Heusler alloy Mn_2VAl (MVA) [16,17,22–25], which has a Curie temperature of 768 K and saturation magnetization (M_s) smaller than that of most Co-based Heusler alloys due to its ferrimagnetic ordering. The small M_s of ferrimagnetic Heusler alloys is beneficial for reducing the critical current density for magnetization switching by STT, which is ideal for low-power operation. Moreover, MVA is expected to possess high negative spin polarization that originates from the electronic structure with a gap in the majority-spin state at the Fermi energy (E_F) [18,21]. Negative P denotes that the spin momentum direction of spin-polarized conduction electrons is opposite to the net magnetization direction. This behavior is opposite to that exhibited by Co-based Heusler alloys with high positive P, whose electronic structure has a gap in the minority-spin state at E_F. Negative P materials exert an STT with torque direction opposite to that seen in positive P materials, which can increase the design freedom of STT-based devices beyond the limits of conventional positive P materials. Device structures that use negative P materials have been proposed for energy-assisted writing in hard disk drive (HDD) applications [33–38]. Furthermore, the small M_s of MVA results in a small disturbance in the writing field of the write head of an HDD, making MVA a very suitable candidate for this application.

Until now, negative P values have been studied primarily by measuring negative MR in MR devices that combine a positive and a negative P material, where the measured resistance becomes

high (low) for the parallel (antiparallel) magnetization configuration. This is the opposite to that occurs in a standard MR device comprising two positive *P* materials. In giant MR (GMR) studies, CoFeGd, FeCr, FeV, NiCr, and Fe_4N have been reported to exhibit negative MR [39–44]. However, the amplitude of the negative MR ratio was less than 1% at room temperature in the case of pseudo-spin-valve current-perpendicular-to-plane GMR (CPP-GMR) devices, indicating the low negative *P* of these devices. Recently, we demonstrated a relatively large negative MR of −1.8% in Mn_2VGa, which has the same crystal structure and magnetic ordering as MVA [27]. The large negative MR of Mn_2VGa indicates high potential of Mn-based Heusler alloys. Moreover, negative *P* materials have been studied for fabricating tunnel MR (TMR) devices, and they show a larger negative MR ratio than those used in GMR devices [26,45,46]. The controllability of the STT direction by negative *P* materials makes these types of materials more attractive as a source of STT rather than a source of MR. In this respect, these materials are more suitable in GMR devices as such devices induce a stronger STT than TMR devices owing to their higher current tolerance. However, only a few studies have investigated the STT of negative *P* materials [41,44]. Therefore, implementing high negative *P* in GMR devices and evaluating the STT effect is critical to the development of spintronic devices utilizing negative *P*.

In this study, we investigated the potential of MVA as a negative *P* material by examining the effects of thermal treatment and composition on atomic ordering and by evaluating MR and STT properties using CPP-GMR devices. In addition, first-principles calculations were conducted for obtaining the density of states (DOSes), antisite formation energy, and transport properties. High-quality MVA films were fabricated via magnetron sputtering at deposition temperatures of 500°C and 600°C. Off-stoichiometric MVA was found to show improved ordering and reduced number of V_{Mn} antisites, which are crucial in obtaining high negative *P* according to the first-principles calculation. The amplitude of negative MR obtained using CPP-GMR devices increased in off-stoichiometric compositions, and devices with the structure of $Mn_{2.2}V_{0.6}Al_{1.2}$/Ag spacer/CoFe

exhibited a very large negative MR of −4.4%, indicating high negative *P* in MVA. Additionally, STT generation via spin injection from MVA was demonstrated. The evaluated STT efficiency was higher than that of FeCr, one of the widely studied negative *P* materials, demonstrating the advantage of MVA.

II. Experimental and computational methods

The DOSs of *B*2- and $L2_1$-ordered MVA were calculated using the density functional theory (DFT) and Korringa–Kohn–Rostoker method offered in the Akai-KKR software package [47–49]. Generalized gradient approximation (GGA) was used for estimating the exchange-correlation energy [50], and disordered states were treated within coherent potential approximation. For all these calculations, we used a lattice constant of a = 5.875 Å. Brillouin-zone integrations for the self-consistent field and DOS calculations were performed using 16 × 16 × 16 and 25 × 25 × 25 *k*-points. The imaginary part of energy for the DOS calculation was set to 0.00005 Ry. Formation energies were calculated by means of the DFT implemented in the Vienna ab initio simulation program [51]. We calculated the formation energy $E_f(X)$ of each defect X using the equation $E_f(X) = E_{\mathrm{tot}}(X) - E_{\mathrm{tot}}(\mathrm{Mn_2VAl}) + \sum_i n_i\mu_i$ [52,53], where $E_{\mathrm{tot}}(X)$ is the total energy of the supercell, including defect X, and $E_{\mathrm{tot}}(\mathrm{Mn_2VAl})$ is the total energy of antisite-free MVA in an equivalent supercell. A MVA supercell contained 32 atoms. The difference between this number of atoms and that of the stoichiometric composition is considered to be n_i = +1 (−1) for an excess (deficiency) of element i, and μ_i is its chemical potential. In this study, we used the values of μ_{Mn}, μ_{V}, and μ_{Al} derived from the energies of α-Mn, body-centered cubic V, and face-centered cubic Al, respectively. We adopted the GGA for yielding the exchange-correlation energy and used projected augmented wave pseudopotential [54,55] to properly investigate the effect of core electrons. The Brillouin-zone integration was performed with 8 × 8 × 8 *k*-points for each supercell.

First-principles calculations for ballistic transmittance based on the Landauer formula [56] were performed using the QUANTUM ESPRESSO code [57,58]. For the exchange-correlation energy, we adopted the ultrasoft pseudopotential method and GGA [50]. A set of 10 × 10 × 1 grids of *k*-points was used for Brillouin-zone integrations. Cutoff energies for the wave function and charge density were set to 40 (Ryd) and 400 (Ryd), respectively. Stacking models of MVA/spacer/MVA (001), where spacer materials were Ag, V, and Cr, were constructed using tetragonal supercells, with the in-plane lattice parameter of the supercell set to 4.061 Å. The interface of the MVA/spacers (001) featured two types of termination: Mn and VAl terminations. Additionally, Al terminations were considered specifically for the Ag spacer. Stacking models comprised seven atomic layers that contained all spacers, with the 17, 15, and 15 atomic layers of MVA being employed for the Mn, VAl, and Al terminations, respectively.

Three types of MVA samples were prepared on MgO (001) substrates via magnetron sputtering. The order of layers in each sample was from bottom to top, and numbers shown in parentheses indicate their thicknesses in nanometers. Single-layer MVA films (type-A sample) consisted of MVA (35)/Ru (2), where the Ru layer serves as a passivation layer. CPP-GMR stacks for MR measurements (type-B samples) consisted of Cr(5)/Ag(100)/Cr(5)/W(5)/MVA(10)/Ag(5)/$Co_{50}Fe_{50}$(7)/Ru(8). CPP-GMR stacks for STT measurements (type-C samples) consisted of Cr(5)/Ag(100)/Cr(5)/W(5)/MVA(15)/Ag(5)/$Fe_{20}Ni_{80}$(5)/Ru(8). MVA layers were grown by the co-sputtering of Mn, V, and Al targets. The MVA composition was controlled by changing the sputtering power and measured via X-ray fluorescence (XRF) analysis calibrated with standard samples whose composition was analyzed using inductively coupled plasma mass spectrometry. The MVA layer was deposited either at an elevated substrate temperature (T_s) or at room temperature and then subsequently annealed at a post-annealing temperature (T_p). The layers above the MVA layer were deposited at room temperature after the sample had cooled down. In

the type-A samples, the following eight MVA compositions were prepared: Mn_2VAl, $Mn_{2.2}V_{0.8}Al$, $Mn_{1.8}V_{1.2}Al$, $Mn_2V_{1.2}Al_{0.8}$, $Mn_2V_{0.8}Al_{1.2}$, $Mn_{2.2}VAl_{0.8}$, $Mn_{1.8}VAl_{1.2}$, and $Mn_{2.2}V_{0.6}Al_{1.2}$. In the type-B and type-C samples, selected compositions were used. Table 1 shows the XRF compositions of the type-A samples deposited at T_s = 600°C, showing that the deviation between the nominal and actual compositions is less than 1.3%. The compositions used in the type-A, B, and C samples are shown in Table 1.

Table 1. Compositions of MVA samples measured via XRF analysis.

	Nominal composition	XRF composition of type-A samples with T_s = 600°C			Type-A samples	Type-B samples	Type-C samples
		Mn (at%)	V (at%)	Al (at%)			
1	Mn_2VAl	49.26	25.97	24.77	✓	✓	
2	$Mn_{2.2}V_{0.8}Al$	54.54	20.90	24.57	✓	✓	
3	$Mn_{1.8}V_{1.2}Al$	43.98	30.72	25.30	✓		
4	$Mn_2V_{1.2}Al_{0.8}$	48.76	31.13	20.11	✓		
5	$Mn_2V_{0.8}Al_{1.2}$	49.73	20.24	30.03	✓	✓	
6	$Mn_{2.2}VAl_{0.8}$	54.66	25.67	19.68	✓		
7	$Mn_{1.8}VAl_{1.2}$	45.11	25.25	29.63	✓		
8	$Mn_{2.2}V_{0.6}Al_{1.2}$	54.25	15.70	30.05	✓	✓	✓

The crystal structure and atomic ordering of the prepared films were investigated via laboratory X-ray diffraction (lab-XRD) with a Cu–$K\alpha$ radiation source. The degrees of the $B2$ and $L2_1$ orders (S_{B2} and S_{L2_1}) were calculated as $S_{B2} = \sqrt{\frac{I_{002}^{exp}/I_{004}^{exp}}{I_{002}^{sim}/I_{004}^{sim}}}$ and $S_{L2_1} = \sqrt{\frac{I_{111}^{exp}/I_{444}^{exp}}{I_{111}^{sim}/I_{444}^{sim}}}$, where I_{hkl}^{exp} and I_{hkl}^{sim} represent the experimental and simulated *hkl* peak intensities, respectively [59,60]. In the XRD simulation model of the off-stoichiometric composition, abundant elements simply occupy the site of deficient elements. In addition, anomalous X-ray diffraction (AXRD) measurements that can distinguish Mn and V with close atomic number were conducted at BL13XU in SPring-8 to quantitatively analyze site occupation [61,62]. The 004 and 111 diffraction peaks were measured at energy around the Mn *K*-absorption edge (6.539 keV) and corrected with respect to the Lorentz factor, self-absorption, and area. The experimental integrated intensities were then compared with simulated $|F_{hkl}|^2$. Here, F_{hkl} is the structural factor of the *hkl* diffraction peak and expressed as

follows: $F_{004} = 2f_X + f_Y + f_Z$ and $F_{111} = f_Y - f_Z$, where f_X, f_Y, and f_Z are the energy-dependent atomic scattering factors of the *X* (Mn), *Y* (V), and *Z* (Al) sites, respectively. The magnetic properties of MVA were evaluated by measuring the magnetization (*M*) versus in-plane magnetic field (*H*) curves using a vibrating sample magnetometer at room temperature. M_s was calculated from the *M* values estimated at sufficiently high *H*, and the sample thickness was estimated using X-ray reflectivity.

The type-B and type-C samples were processed in pseudo-spin-valve CPP-GMR devices using the following procedure. First, thin films were patterned into circular pillars with a diameter of 80 nm via electron-beam lithography and Ar-ion milling. After patterning, the pillars were covered with a thin Ta adhesion layer and a SiO_2 passivation layer. After the lift-off of the covering layers, a Au top electrode was fabricated. A total of 150 devices were prepared on one sample. Resistance versus in-plane magnetic field (*R*–*H*) measurements were conducted using the four-probe method. All devices were measured with an auto-prober system that has an *H* range of 0.25 T at room temperature. Few of these devices were additionally analyzed using a physical property measurement system (PPMS) at lower temperatures. The MR ratio was defined as $MR = (R - R_{\mathrm{max}})/R_{\mathrm{max}}$, where R_{max} is the maximum *R* in the measured *H* range. Note that this definition differs from the conventional definition using parallel and antiparallel resistances because the parallel resistance was not always measurable because MVA magnetization was not saturated in the *H* direction in the measured *H* range and antiparallel resistance was not measurable because the complete antiparallel configuration was not obtained owing to the gradual change in MVA magnetization.

The STT measurements of type-C samples were conducted on circular devices with a diameter of 80 nm using the PPMS. This method is described in great detail in Ref. [44]. First, a sufficient perpendicular field (H_z) was applied to saturate the MVA and NiFe magnetic layers in the

perpendicular direction. Then, R was measured by sweeping the bias current (I_b). Positive I_b was defined as the current flow from top to bottom. By applying sufficient I_b, NiFe magnetization reverses against H_z due to the STT induced by spin injection from the MVA layer, and this magnetization reversal was reflected as the R change through the MR effect. The R–I_b curves were fitted phenomenologically using $R = f(I_b) + \frac{\Delta R}{2}\left(1 + \mathrm{erfc}\left(\frac{I_b - I_c}{I_{width}}\right)\right)$. Here, f is a second-order polynomial function representing the R change due to the Joule heating by applying I_b, ΔR represents the R change due to magnetization reversal, erfc is the error function, and critical current (I_c) corresponds to the I_b value at the center of the R change. I_{width} represents the I_b width of the R change, and approximately 85% of the R change occurs in the range of $I_c \pm I_{width}$.

The cross-sectional microstructure of samples was analyzed using high-angle annular dark-field scanning transmission electron microscopy (HAADF-STEM), nano-beam electron diffraction (NBED), and energy-dispersive X-ray spectroscopy (EDS).

III. Results and discussions

A. First-principles calculations of DOSs and formation energies of antisites and vacancies

Figure 1(a) shows the energy dependence of DOSs for $L2_1$- and $B2$-ordered Mn_2VAl together with P at E_F and M_s. Both results exhibit a gap structure around E_F in the majority-spin state. The resulting negative P is very high (−95%) for the $L2_1$-ordered state and decreases to −76% for the $B2$-ordered state, indicating that the $L2_1$-ordered state is desirable for obtaining a higher negative P. Additionally, we investigated the effect of off-stoichiometry on P by changing the Mn/V ratio because these two elements primarily determine the ferrimagnetic and spintronic properties of MVA. Figure 1(b) shows the energy dependence of the DOS for $L2_1$-ordered $Mn_{2.2}V_{0.8}Al$ and $Mn_{1.8}V_{1.2}Al$. The Mn-rich composition maintains the gap structure with a slightly smaller negative

203 *P* than that observed in the stoichiometric case. In contrast, an in-gap state appears in the V-rich
204 composition, considerably decreasing negative *P*. The effect of V_{Mn} antisites on negative *P* has
205 also been reported in the case of Mn_2VGa, which has a similar DOS with a gap in the majority-
206 spin state [26–28]. Additionally, calculations were performed for the MVA compositions of
207 $Mn_2V_{0.8}Al_{1.2}$ and $Mn_{2.2}V_{0.6}Al_{1.2}$ as they exhibit higher ordering in the experimental results, which
208 we discuss later. In these compositions, the energy gap is maintained with a *P* of approximately
209 −80%. In all compositions except for $Mn_{1.8}V_{1.2}Al$, the calculated M_s is close to the following
210 values estimated from the Slater–Pauling rule: 2 μ_B/f.u. (Mn_2VAl and $Mn_{2.2}V_{0.6}Al_{1.2}$), 1.6 μ_B/f.u.
211 ($Mn_{2.2}V_{0.8}Al$), and 2.4 μ_B/f.u. ($Mn_2V_{0.8}Al_{1.2}$). For $Mn_{1.8}V_{1.2}Al$, the deviation in the calculated M_s
212 from the Slater–Pauling value of 2.4μ_B/f.u. is relatively large, which coincides with the
213 deterioration in the gap structure.
214
215 We calculated the formation energies of antisites and vacancies in MVA to gain insight into site
216 occupation in off-stoichiometric samples, as shown in Table 2. The formation energy of the Mn
217 vacancies is higher than those of the V_{Mn} and Al_{Mn} antisites, indicating that in Mn-deficient
218 compositions, V or Al atoms occupy the Mn site instead of forming Mn vacancies. Similarly, V
219 and Al vacancies are not expected to form because of their high formation energies. For
220 comparison, we refer to the case of Co_2MnSi [53,63]. In this system, the formation energy of
221 Co_{Si} antisites is very high (2.25 eV and 2.3 eV), which rules out this type of antisite formation
222 and helps to predict site occupation in off-stoichiometric compositions. Here, the first value
223 presented in parentheses is adopted from Ref. [53], and the second is from our own calculation
224 of the same system. Contrary to studies on Co_2MnSi, in this study, we do not rule out any specific
225 types of antisites in MVA because all antisites similarly have relatively small formation energies.
226 The formation energies of V_{Al} and Al_V are especially small, suggesting that disorder between
227 these two atoms can easily occur in MVA.
228

Table 2. Formation energies of antisites and vacancies.

	Formation energy (eV)
Mn_V antisite	0.93
Mn_{Al} antisite	0.85
V_{Mn} antisite	0.73
V_{Al} antisite	0.37
Al_{Mn} antisite	0.58
Al_V antisite	0.29
Mn vacancy	2.1
V vacancy	3.0
Al vacancy	3.9

B. Growth of single-layer MVA: effect of thermal treatment and composition tuning

In this section, we discuss the growth of MVA as a result of different thermal treatments and varying composition. Figure 2(a) shows the out-of-plane XRD profiles of the type-A stoichiometric Mn_2VAl samples prepared at T_s = 300ºC–600ºC and T_p = 500ºC–600ºC. All results show only the diffraction peaks related to the (001) plane, indicating (001)-oriented growth. At elevated deposition temperatures, the 002 superlattice peaks implying the presence of the *B*2 order were not observed at T_s = 300ºC, have appeared very faintly at T_s = 400ºC, and were clearly observable at T_s = 500°C and 600ºC. In post-annealing samples, the 002 peak appeared clearly at T_p =600ºC. Figure 2(b) shows the corresponding XRD profiles along the [111] direction at χ = 54.7°. The 111 superlattice peaks indicate the presence of the $L2_1$ order, and they appeared only for samples where T_s = 500ºC–600ºC or T_p = 600ºC. In all the samples, no peaks other than those associated with the full-Heusler crystal phase were observed, showing that single-phase MVA films were obtained at all temperatures. Figure 2(c) shows the T_s and T_p dependence of S_{B2} and S_{L2_1}. The S_{B2} value was 0.7 at 500ºC and increased to 0.88 at 600ºC. Meanwhile, the S_{L2_1} value was approximately 0.5 at 600ºC. In post-annealed samples, S_{B2} and S_{L2_1} were smaller than those observed for elevated temperature deposition samples, indicating that the latter approach achieves the better ordering of MVA. The small S_{L2_1} was consistent with the calculated formation energies of antisites, implying that the mixing of V and Al can occur easily. Figure 2(d) shows the T_s and

249 T_p dependence of M_s. M_s showed a similar trend to that seen for order parameters. The
250 experimental values were smaller than the Slater–Pauling value of 2 μ_B/f.u., reflecting disorder in
251 our films.
252
253 In addition to stoichiometric samples, we also prepared off-stoichiometric samples. Based on
254 the results of the thermal treatment study, T_s = 500ºC and 600ºC were used to obtain high ordering.
255 For each sample, two among Mn, V, and Al atoms were selected, and their balance changed by
256 ±0.2, resulting in samples 2–7, as listed in Table 1. Additionally, a $Mn_{2.2}V_{0.6}Al_{1.2}$ sample was
257 prepared. We confirmed the (001)-oriented single-phase growth of MVA for all compositions
258 using XRD (selected data are later shown in Fig. 4). Figure 3(a) shows a bar graph for the M_s of
259 the type-A samples with different compositions. The M_s values show clear composition
260 dependence, but they do not change significantly for each composition when the temperature is
261 varied between T_s = 500ºC and 600ºC. In Fig. 3, we also introduced a parameter, M_s ratio, which
262 is defined as the experimental M_s normalized by the M_s calculated based on the Slater–Pauling
263 rule. The M_s ratio is expected to be close to unity when the gap in the electronic structure is
264 preserved and there is no disorder in MVA [20]. Here, the temperature effect on M_s was neglected
265 considering the high Curie temperature of MVA. The right-hand side vertical axis of Fig. 3(a)
266 shows the M_s ratio for samples with T_s = 600ºC using a circle symbol. M_s ratios higher than that
267 of the stoichiometric composition were obtained for the following compositions in the ascending
268 order: Mn-rich V-deficient composition ($Mn_{2.2}V_{0.8}Al$), Al-rich V-deficient composition
269 ($Mn_2V_{0.8}Al_{1.2}$), and the combination of these two ($Mn_{2.2}V_{0.6}Al_{1.2}$). These results suggest that these
270 compositions can promote better ordering than that is achievable with the stoichiometric
271 composition. Note that the calculated DOS demonstrates that these off-stoichiometric
272 compositions possess relatively high negative P. Figure 3(b) shows the in-plane M–H curves for
273 type-A samples (T_s = 600ºC) of Mn_2VAl, $Mn_{2.2}V_{0.8}Al$, $Mn_2V_{0.8}Al_{1.2}$, and $Mn_{2.2}V_{0.6}Al_{1.2}$. The M–
274 H curve for Mn_2VAl displays a gradual change over a wide H range of ±0.5 T with a coercive

field (H_c) of ~65 mT. The *M*–*H* curve for $Mn_{2.2}V_{0.8}Al$ is similar to that for Mn_2VAl. For Al-rich compositions ($Mn_2V_{0.8}Al_{1.2}$ and $Mn_{2.2}V_{0.6}Al_{1.2}$), M_s increases and H_c decreases to ~40 mT, with magnetization curves showing improved squareness.

Figure 4(a) shows the out-of-plane XRD profiles for type-A samples (T_s = 600ºC) of Mn_2VAl, $Mn_{2.2}V_{0.8}Al$, $Mn_2V_{0.8}Al_{1.2}$, and $Mn_{2.2}V_{0.6}Al_{1.2}$. The 004 and 002 reflections were observed in all four samples, indicating the single-phase (001)-oriented growth and presence of *B*2 ordering. Figure 4(b) shows the intensity ratio of the 002 peak over the 004 peak. The intensity ratios for the $Mn_2V_{0.8}Al_{1.2}$ and $Mn_{2.2}V_{0.6}Al_{1.2}$ samples were found to increase in comparison with the stoichiometric and $Mn_{2.2}V_{0.8}Al$ compositions. This increase in the intensity ratio for the Al-rich compositions is explained by the fact that the intensity of the 002 reflection primarily depends on the amount of Al in the V–Al plane as the atomic scattering factors of Mn (Z = 25) and V (Z = 23) are similar and that of Al (Z = 13) is smaller. As seen in the right-hand axis of Fig. 4(b), we calculated the S_{B2} ordering parameter considering the off-stoichiometry. S_{B2} increases for the Al-rich compositions. Because all four samples have a stoichiometric or a slightly Mn-rich content, the higher *B*2 ordering indicates that the *X* site is more dominantly occupied by Mn atoms, with the smaller numbers of V and Al atoms occupying this site. Considering that V_{Mn} antisites significantly influence the negative *P* of this Heusler alloy, MVA films with their *X* sites occupied primarily by Mn atoms are expected to have high negative *P*.

To further improve our understanding of the type of disorder and reveal site occupation in our samples, we conducted AXRD measurements on type-A samples (T_s = 600ºC) of Mn_2VAl, $Mn_{2.2}V_{0.8}Al$, and $Mn_2V_{0.8}Al_{1.2}$. Figures 5(a) and 5(b) show the X-ray energy dependence of the 004 and 111 reflections obtained around the Mn *K*-absorption edge, respectively. The energy profile of the 004 peak shows a dip at the Mn *K*-absorption edge for all compositions in a similar manner. The energy profile of the 111 peak is almost flat for Mn_2VAl and $Mn_2V_{0.8}Al_{1.2}$ but shows

a dip for $Mn_{2.2}V_{0.8}Al$. The experimental results were analyzed by fitting them using simulations. We introduced parameters *A* and *B*, which represent the fractions of disorder between Mn atoms in the *X* site and V atoms in the *Y* site as well as Mn atoms in the *X* and Al atoms in the *Z* site, respectively. Initially, disorder between the *Y* and *Z* sites is first neglected. Then, the atomic scattering factors of the *X*, *Y*, and *Z* sites of the Mn_2VAl sample are expressed as follows: $F_X = \left(\frac{49.26}{50} - A - B\right) f_{\mathrm{Mn}} + \left(\frac{0.74}{50} + A\right) f_{\mathrm{V}} + B f_{\mathrm{Al}}$, $F_Y = A f_{\mathrm{Mn}} + (1 - \mathrm{A}) f_{\mathrm{V}}$, and $F_Z = B f_{\mathrm{Mn}} + \frac{0.23}{25} f_{\mathrm{V}} + \left(\frac{24.77}{25} - \mathrm{B}\right) f_{\mathrm{Al}}$, where f_{Mn}, f_{V}, and f_{Al} are the atomic scattering factors of each element. Three sets of values were used for *A* and *B* to find the best fit, (0, 0.07), (0.06, 0.06), and (0.15, 0.04), which all reproduce the S_{B2} value of 0.88 observed in lab-XRD. The range of *B* is smaller than that of *A* because the 002 reflection is more sensitive to *B* due to the larger difference in the atomic scattering factor between Mn and Al than that between Mn and V. Figure 5(c) shows the simulated curve for the 004 reflection of the stoichiometric Mn_2VAl sample. In the case of the 004 peak, simulated curves are the same regardless of the values of *A* and *B* because the 004 peak reflects the summation of the scattering factors of each site. The simulated curves reproduce the experimental energy profile, demonstrating the accuracy of the simulation. Figure 5(d) shows the simulated 111 reflection intensity based on the XRF composition of the Mn_2VAl and $Mn_{2.2}V_{0.8}Al$ samples. Depending on *A* and *B* values, simulated curves for the stoichiometric sample show either a convex, flat, or concave energy profile. Because the 111 peak intensity was determined based on the difference in the scattering factor between the *Y* and *Z* sites, a peak (dip) appears when the *A* (*B*) parameter is higher than the other one while the profile becomes flat for *A* = *B*. For the stoichiometric Mn_2VAl sample, the experimental 111 reflection profile is almost flat, which is consistent with the simulated curve for *A* = 0.06 and *B* = 0.06. These results indicate that there is no clear preference in the formation of Mn–V and Mn–Ga disorders in MVA, as suggested earlier when discussing the formation energy of different disorder types in MVA. In the case of Mn-rich $Mn_{2.2}V_{0.8}Al$, the 111 profile shows a dip, indicating that the excess Mn atoms

preferentially occupy the empty V sites. The simulated curve for the $Mn_{2.2}V_{0.8}Al$ sample where A = 0.1 and B = 0.06 (calculated from S_{B2} = 0.85 observed via XRD) reproduces its experimental profile. Similar to the stoichiometric sample, the flat profile obtained for the $Mn_2V_{0.8}Al_{1.2}$ sample indicates that the amount of Mn–V and Mn–Ga disorders present in this sample is similar.

We now consider disorder between the Y and Z sites. Note that this type of disorder changes the 111 peak intensities but does not affect the shape of the energy profile. By applying Y–Z disorder to the AXRD analysis to satisfy the conditions needed to obtain S_{L2_1} observed via XRD, site occupation was determined as follows: $[Mn_{1.85}V_{0.09}Al_{0.06}][Mn_{0.06}V_{0.71}Al_{0.23}][Mn_{0.06}V_{0.24}Al_{0.7}]$ for Mn_2VAl, $[Mn_{1.84}V_{0.1}Al_{0.06}][Mn_{0.22}V_{0.55}Al_{0.23}][Mn_{0.12}V_{0.19}Al_{0.69}]$ for $Mn_{2.2}V_{0.8}Al$, and $[Mn_{1.91}V_{0.04}Al_{0.05}][Mn_{0.04}V_{0.71}Al_{0.25}][Mn_{0.04}V_{0.06}Al_{0.9}]$ for $Mn_2V_{0.8}Al_{1.2}$. Notably, the Al-rich composition has the smallest number of V_{Mn} antisites.

The anisotropic magnetoresistance (AMR) was measured for type-A samples (T_s = 600ºC) of Mn_2VAl, $Mn_{2.2}V_{0.8}Al$, $Mn_2V_{0.8}Al_{1.2}$, and $Mn_{2.2}V_{0.6}Al_{1.2}$ (data are shown in the Supplemental Material [64]). All the MVA samples exhibit positive AMR ratios for the current along the MVA [110] direction, and negative ratios for the current direction along the MVA [100] direction. Such sign reversal by the current direction was reported in the case of Mn_2VGa and analyzed from the viewpoint of DOS, and the analysis result supported the negative P of Mn_2VGa [28]. The similar AMR behavior observed in Mn_2VGa and MVA supports that these materials have similar electronic band structure with negative P. The amplitude of the AMR ratio changed with the composition, and the change was especially large for $Mn_{2.2}V_{0.6}Al_{1.2}$, implying the modification in the electronic band structure by the composition tuning.

C. Negative MR in CPP-GMR devices

In this section, we discuss the fabrication of CPP-GMR devices and investigate their MR properties. Figure 6(a) shows the stacking structure of the type-B samples used to fabricate CPP-GMR devices. The MVA layer compositions were Mn_2VAl, $Mn_{2.2}V_{0.8}Al$, $Mn_2V_{0.8}Al_{1.2}$, and $Mn_{2.2}V_{0.6}Al_{1.2}$. The deposition temperature was T_s = 500ºC as this temperature achieved a flat surface with an average roughness (R_a) of approximately 0.3 nm. For T_s = 600ºC, the roughness increased to R_a = 1.2 nm. Each MVA layer was grown on a Cr/W buffer layer. In our previous study of CPP-GMR using Mn_2VGa, we found that these buffer layers were effective in suppressing the diffusion of Mn_2VGa [27]. Figure 6(b) shows an example of *R*–*H* curves for Mn_2VAl. The behavior of the *R*–*H* curve in the case of the downward *H* sweep can be understood based on the schematics of the magnetization configuration shown above the figure. As seen in the *M*–*H* curves in Figure 3(b), MVA magnetization changes gradually while the CoFe layer switches at around the zero field. The abrupt change in *R* seen in Figure 6(b) corresponds to the magnetization switching of the CoFe layer, and afterward, the trend of the *R* change alters from negative to positive. This result implies that *R* is higher (lower) when the magnetization configuration of the CoFe and MVA layers is more parallel (antiparallel), and the maximum MR ratio reaches −1.5%. A negative MR indicates negative *P* in the MVA layer because the bulk spin asymmetry of CoFe and interfacial spin scattering asymmetry of CoFe/Ag are positive [65]. Owing to the incomplete antiparallel configuration of devices resulting from the gradual change in MVA magnetization, the full MR ratio could not be evaluated.

Figures 6(c)–6(e) show an example of the *R*–*H* curve for the $Mn_{2.2}V_{0.8}Al$, $Mn_2V_{0.8}Al_{1.2}$, and $Mn_{2.2}V_{0.6}Al_{1.2}$ samples, respectively. Negative MR is observed in all three compositions. Figure 6(f) shows a summary of the MR ratios obtained from all devices for each sample. Defective devices that showed abnormal *R* were excluded. The shapes of *R*–*H* curves exhibit device-to-device variations within each sample because of the incomplete antiparallel configuration of devices. Namely, devices with a more antiparallel magnetization configuration near the zero field

exhibit a larger negative MR. Another possible reason for this variation in the magnitude of MR is the spatialy nonuniform ordering within the thin film of each sample. The negative MR ratio is statistically enhanced using off-stoichiometric compositions, reaching a maximum of −4.4 % for the $Mn_{2.2}V_{0.6}Al_{1.2}$ sample. This enhancement in the negative MR is consistent with the high M_s ratio observed for these compositions, demonstrating that improved ordering via composition tuning increases negative P in MVA. The resistance area (RA) product is calculated to be 24 $m\Omega\cdot\mu m^2$. Figure 6(g) shows the temperature dependence of the MR ratio for $Mn_{2.2}V_{0.6}Al_{1.2}$. The negative MR ratio increases as the temperature is reduced, reaching a maximum of −7.9%.

D. STT in CPP-GMR devices

We next investigated STT induced via spin injection from the MVA layer. Figure 7(a) shows the stacking structure of the type-C samples used for the STT measurement. Compared with the type-B samples, the upper magnetic layer in the type-C sample was changed from CoFe to NiFe to reduce M_s. This is necessary to induce the magnetization reversal of this layer using STT within the I_b tolerance of the device. Furthermore, the MVA layer thickness was increased to stabilize MVA magnetization against STT. Based on the results presented in the previous section, the MVA layer composition was adjusted to $Mn_{2.2}V_{0.6}Al_{1.2}$ and a deposition temperature of T_s = 500ºC was used. Figure 7(b) shows an example of the R–H curve. Similar to the results presented in the previous section, negative MR was observed. Compared with the type-B samples, the amplitude of the negative MR ratio was smaller, decreasing to −1.8% due to the different upper magnetic layer. Figure 7(c) shows R–I_b curves measured at several H_z values. The H_z values were large enough to align MVA and NiFe magnetizations along the field direction at zero bias. R–I_b curves exhibit an overall parabolic increase due to Joule heating. Additionally, R–I_b curves show a decrease in the positive I_b region when sufficient I_b was introduced. This decrease in R is attributed to magnetization reversal detected through the negative MR.

In the following, we deduce that magnetization reversal occurs in the NiFe layer and not in the MVA layer. The layer that exhibits magnetization reversal was not determined solely by the I_b direction because the injection of transmitted spin from the MVA layer with negative P and injection of reflected spin from the NiFe layer with positive P enable STT to reverse the magnetization of the opposite layer in the positive I_b region. The STT required for magnetization reversal is proportional to the magnetic volume, defined as the product of M_s and thickness, and Gilbert damping constant (α). Although the MVA layer was three times as thicker as the NiFe layer, which was intended to stabilize MVA magnetization against spin injection, the magnetic volume of the MVA layer was calculated to be 4.8 nm T and was similar to that of the NiFe layer (4.5 nm·T) because of the smaller M_s of MVA. However, the α value of $Mn_{2.2}V_{0.6}Al_{1.2}$ was 0.025, which was larger than that of NiFe whose α was 0.011. This indicates that MVA magnetization was more stable against STT than NiFe magnetization, suggesting that magnetization reversal occurred in the NiFe layer. The α value was estimated from the ferromagnetic resonance measurement of the type-A sample of $Mn_{2.2}V_{0.6}Al_{1.2}$ (data are shown in the Supplemental Material [64]), and high α observed in MVA has been reported previously [24]. To be more precise, the STT efficiency of each layer needs to be considered, which we discuss later.

To compare STT induced by materials with negative and positive P, we show results for an identical set of measurements conducted for a CPP-GMR device in which the lower magnetic layer was replaced with $Co_2FeGa_{0.5}Ge_{0.5}$ (CFGG), with high positive P. The results are from Ref. [66] and shown in the inset in Fig. 7(c). The layer structure of the CPP-GMR device was Cr(5)/Ag(100)/CFGG(15)/Ag(7)/$Fe_{20}Ni_{80}$(7.5)/Ru(8), and the post-annealing of the sample was performed at 500°C after the deposition of the CFGG layer. The increase in R due to magnetization reversal appeared in the negative I_b region. Because NiFe and CFGG have positive P, the current direction determined that magnetization reversal occurred in the NiFe layer. The

magnetization reversal of the CFGG layer was not detected in the positive I_b region in the measured range because of its large magnetic volume. This comparison clearly shows that I_b polarity for the magnetization reversal of the Heusler alloy was opposite for MVA and CFGG, reflecting the opposite sign of P in these two materials.

In addition, the dependence of STT on the relative angle between two magnetic layers could be seen in this comparison. The I_{width} values estimated by fitting were approximately 0.52 mA for the CFGG device and 2.2 mA for the MVA device at $\mu_0 H_z$ = 2.2 T, which indicated that magnetization reversal occurred more abruptly with I_b for CFGG than that for MVA. When both the magnetic layers have positive P, the angle dependence of STT efficiency was lower (higher) near the parallel (antiparallel) configuration [67]. Therefore, after commencing magnetization reversal from the parallel configuration (zero angle), the STT efficiency increased with the increase of the magnetization angle, which resulted in abrupt magnetization reversal, corresponding to the small I_{width} of the device using CFGG. Meanwhile, when the two magnetic layers have positive and negative P values, the STT efficiency exhibited the opposite angular dependence [67], resulting in gradual magnetization reversal that corresponds to the large I_{width} of the MVA device.

According to theory, when the magnetization is near the equator in the middle of magnetization reversal at a certain current density, the damping and STT of the system balance out. The critical current density J_c that satisfies this balance is expressed as

$$J_c = \mu_0 \frac{2|e|}{\hbar \eta} \alpha M_s^{NiFe} d H_{eff}. \quad (1)$$

Here, d = 5 nm is the thickness, M_s^{NiFe} is the M_s of the NiFe layer, and α = 0.011 is the damping constant of the NiFe layer. $\hbar$ is Planck's constant, and e is the elementary charge. The effective field H_{eff} includes H_z, the demagnetizing field of the NiFe layer, and the dipolar field from the MVA layer, all of which have only a z-direction component on average because of the circular pillar shape of the device. This equation means that J_c depends linearly on H_z and that STT efficiency η can be estimated from the slope of this linear relationship. We assumed that NiFe magnetization was on the equator at I_c, which was estimated from fitting the R–I_b curves. Figure 7(d) shows the dependence of I_c on H_z. In addition to the data shown in Fig. 7(c), data from other devices fabricated on the same sample were measured and are shown on the same graph. A clear linear dependence was observed in multiple devices, which is consistent with the theoretical model. From the slope, η was estimated to be −0.72. This value is much higher than −0.15 reported for FeCr [44], demonstrating that MVA with high negative P could induce larger STT. Furthermore, the η value in the MVA layer was higher than that in the NiFe layer, indicating that STT induced by the MVA layer, which acts upon the NiFe layer, was stronger than that of NiFe acting upon MVA. The higher STT efficiency of the MVA layer, together with its higher stability, verified that magnetization reversal occurred only in the NiFe layer.

E. Cross-sectional TEM of GMR stacks

We conducted cross-sectional TEM to confirm that the designed GMR stacks were properly fabricated. Figures 8(a) and 8(b) show the HAADF-STEM image and corresponding EDS mapping of the type-B sample with a $Mn_{2.2}V_{0.6}Al_{1.2}$ layer, respectively. In the EDS mapping, only the Fe signal from the CoFe layer and the Mn signal from the MVA layer are shown for simplicity. The STEM and EDS results confirm sharp and flat interfaces between neighboring layers with no interdiffusion. The layer thicknesses are consistent with the designed values. The inset in Fig. 8(a) shows the NBED patterns obtained for the MVA layer. The 002 and 111 spots are observed in

these patterns, confirming the existence of the $B2$ and $L2_1$ ordering in the thin film, which is consistent with the XRD results shown earlier. Figures 8(c) and 8(d) show the HAADF-STEM images obtained for the MVA/Ag/CoFe and W/MVA/Ag structures, respectively. Atomically sharp interfaces were observed at the CoFe/Ag, Ag/MVA, and MVA/W interfaces, with atomic dislocations being denoted using $\perp$ symbol in these figures. Figure 8(e) shows atomic-resolution EDS elemental maps of Ag, Mn, V, and Al in the MVA/Ag interface. An Al-rich termination layer is formed at the interface. The second layer from the interface consists of Mn, and the third layer consists of alternately arranged V and Al. Below the second layer, the structure is uniform and comprises the alternate stacking of a Mn-rich layer and the V- and Al-rich layers, indicating the presence of the $L2_1$ structure in the MVA film.

F. Transmittance calculations

We calculated the transmittance of the MVA/spacer/MVA (001) structure to examine the Fermi surface matching of MVA with a spacer and to gain insight into the suitability of different spacer materials with MVA to best utilize the negative P of this material. To find an ideal spacer material, in addition to Ag used previously, we explored transmittance in the V and Cr spacer layers. Figures 9(a)–9(c) show the in-plane wave vector dependence of minority-spin transmittance in the parallel magnetization configuration for the Ag, V, and Cr spacers, respectively. The minority spin was considered here because of the negative P of MVA. The Mn and VAl terminations were considered. For the Ag spacer, the Al termination observed via TEM was also considered, where V atoms in the VAl termination were replaced by Al atoms. Table 3 shows the interfacial RA calculated from transmittance. The V spacer exhibits the lowest interfacial RA, regardless of the termination. The Ag spacer shows a slightly higher interfacial RA than V, and the Cr spacer displays a significantly higher interfacial RA. This result indicates that V is a more suitable spacer material than Ag, which we used in our earlier experiments; furthermore, Cr is not a suitable

spacer material for any MVA devices. For all spacer materials used here, the Mn termination demonstrates a smaller interfacial RA than the VAl termination. In the case of the Al termination for the Ag spacer, the RA value is almost the same as that of the VAl termination.

The results obtained for MVA are now compared with those for a CFGG/Ag/CFGG(001) stack, for which a high MR ratio has been reported experimentally. The interfacial RA of the majority-spin electron in this system is calculated to be 1.77, 1.69, and 2.32 mΩ·μm^2 for the FeGa, FeGe and, Co terminations, respectively. The majority spin was considered because of the positive *P* of $Co_2FeGa_{0.5}Ge_{0.5}$ The interfacial RA is much higher in the MVA/Ag/MVA(001) structure than in the CFGG/Ag/CFGG(001) structure, which partly explains the smaller magnitude of the negative MR ratio in the MVA system than that observed in the system using a Co-based Heusler alloy and a Ag spacer. The high interfacial RA indicates weak hybridization between Ag and Mn (V) orbitals. Although the V spacer shows some promising initial results, further research is necessary to find an optimal spacer material to increase the MR ratio so that it is comparable to the very large MR ratio observed in Co-based Heusler/Ag systems.

Table 3. Interfacial RA of the MVA/spacer/MVA (001) structure

Interfacial RA (mΩ·μm^2)	Mn termination	VAl termination	Al termination
Ag spacer	6.02	6.142	6.130
V spacer	4.288	5.480	-
Cr spacer	9.282	9.975	-

VI. Conclusion

Mn_2VAl Heusler alloy thin films were investigated for spintronic applications utilizing the negative spin polarization of the material. The DOS calculations showed that MVA has a negative *P* due to a gap in the majority-spin state, which is higher in MVA with the $L2_1$ order than in MVA with the *B*2 order. V_{Mn} antisites considerably reduced the negative *P* of the material, while Mn_V

and Al_V antisites in the Mn-rich and Al-rich compositions weakly influenced *P*. These results indicate that improving the ordering and suppressing V_{Mn} antisites are crucial for achieving high negative *P* in MVA. The thermal treatment of MVA was explored to improve the atomic ordering of the material. The *B*2 and $L2_1$ orders were observed in stoichiometric Mn_2VAl samples grown at T_s = 500°C and MVA samples post-annealed at T_p = 600°C. MVA grown at elevated temperatures showed higher order than samples grown via post-annealing. Samples with off-stoichiometric compositions ($Mn_{2.2}V_{0.8}Al$, $Mn_2V_{0.8}Al_{1.2}$, and $Mn_{2.2}V_{0.6}Al_{1.2}$) exhibited better ordering than the stoichiometric sample. Furthermore, the Al-rich composition was found to reduce V_{Mn} antisites. We fabricated GMR stacks comprising MVA/Ag/CoFe, for which TEM analysis revealed sharp and flat interfaces between each layer, without any notable interdiffusion. A negative MR ratio was observed in the fabricated CPP-GMR devices, which provided evidence for negative *P* in MVA, and the amplitude of negative MR increased when employing samples with an off-stoichiometric composition for fabricating devices. A maximum negative MR ratio of −4.4% at room temperature was observed for the $Mn_{2.2}V_{0.6}Al_{1.2}$ sample, which is the largest negative MR ever reported for a pseudo-spin-valve CPP-GMR, indicating the high negative *P* of MVA. In addition, STT induction via spin injection from the MVA layer was demonstrated to be more efficient than that obtained in FeCr. These results demonstrate that MVA is a potential candidate for spintronic applications due to its high negative spin polarization. In particular, the demonstration of efficient STT generation in MVA-based devices is important from an application point of view as negative *P* materials are of interest as an STT source due to their ability to control the direction of torque.

Acknowledgments

Synchrotron XRD measurement were performed with the approval of Japan Synchrotron Radiation Research Institute (JASRI) with the proposal No. 2021A1300 and 2023A1563. The

authors thank Dr. T. Kubota at Tohoku University for fruitful discussions on Mn-based Heusler alloys, Dr. P.D. Bentley at National Institutes for Quantum Science and Technology (QST) for reviewing the English language of this manuscript, and M. Inoue at NIMS for technical support.

Funding

This work was partially supported by the Advanced Storage Research Consortium (ASRC), JSPS KAKENHI (grant numbers 21K20434 and 23K03934], and MEXT Initiative to Establish Next-generation Novel Integrated Circuits Centers (X-NICS) (grant number JPJ011438).

Data availability

The data that support the findings of this study are available from the corresponding author upon reasonable request.

Supplementary Material

The supplemental material presents FMR measurements and anisotropic MR measurements of the single-layer MVA samples.

References

[1] J. C. Slonczewski, *Current-Driven Excitation of Magnetic Multilayers*, J. Magn. Magn. Mater. **159**, L1 (1996).

[2] L. Berger, *Emission of Spin Waves by a Magnetic Multilayer Traversed by a Current*, Phys. Rev. B **54**, 9353 (1996).

[3] S. I. Kiselev, J. C. Sankey, I. N. Krivorotov, N. C. Emley, R. J. Schoelkopf, R. A. Buhrman, and D. C. Ralph, *Microwave Oscillations of a Nanomagnet Driven by a Spin-Polarized Current*, Nature **425**, 380 (2003).

[4] M. Hosomi et al., *A Novel Nonvolatile Memory with Spin Torque Transfer Magnetization Switching: Spin-RAM*, Tech. Dig. - Int. Electron Devices Meet. IEDM **2005**, 459 (2005).

[5] F. Macià, A. D. Kent, and F. C. Hoppensteadt, *Spin-Wave Interference Patterns Created by Spin-Torque Nano-Oscillators for Memory And*, Nanotechnology **22**, 095301 (2011).

[6] J. Torrejon et al., *Neuromorphic Computing with Nanoscale Spintronic Oscillators*, Nat. 2017 5477664 **547**, 428 (2017).

[7] T. Kanao, H. Suto, K. Mizushima, H. Goto, T. Tanamoto, and T. Nagasawa, *Reservoir Computing on Spin-Torque Oscillator Array*, Phys. Rev. Appl. **12**, 024052 (2019).

[8] Y. Sakuraba, M. Hattori, M. Oogane, Y. Ando, H. Kato, A. Sakuma, T. Miyazaki, and H. Kubota, *Giant Tunneling Magnetoresistance in Co2MnSi/Al–O/Co2MnSi Magnetic Tunnel Junctions*, Appl. Phys. Lett. **88**, 192508 (2006).

[9] H. Liu, Y. Honda, T. Taira, K. Matsuda, M. Arita, T. Uemura, and M. Yamamoto, *Giant Tunneling Magnetoresistance in Epitaxial Co2MnSi/MgO/Co2MnSi Magnetic Tunnel Junctions by Half-Metallicity of Co2MnSi and Coherent Tunneling*, Appl. Phys. Lett. **101**, 132418 (2012).

[10] S. Li, Y. K. Takahashi, T. Furubayashi, and K. Hono, *Enhancement of Giant Magnetoresistance by L21 Ordering in Co2Fe(Ge0.5Ga0.5) Heusler Alloy Current-Perpendicular-to-Plane Pseudo Spin Valves*, Appl. Phys. Lett. **103**, 042405 (2013).

[11] M. Jourdan et al., *Direct Observation of Half-Metallicity in the Heusler Compound Co2MnSi*, Nat. Commun. **5**, 3974 (2014).

[12] J. W. Jung, Y. Sakuraba, T. T. Sasaki, Y. Miura, and K. Hono, *Enhancement of Magnetoresistance by Inserting Thin NiAl Layers at the Interfaces in Co2FeGa0.5Ge0.5/Ag/Co2FeGa0.5Ge0.5 Current-Perpendicular-to-Plane Pseudo Spin Valves*, Appl. Phys. Lett. **108**, 102408 (2016).

[13] S. Andrieu, A. Neggache, T. Hauet, T. Devolder, A. Hallal, M. Chshiev, A. M. Bataille, P. Le Fèvre, and F. Bertran, *Direct Evidence for Minority Spin Gap in the <math> <mrow> <mi Mathvariant="normal">C</Mi> <msub> <mi Mathvariant="normal">o</Mi> <mn>2</Mn> </Msub> <mi>MnSi</Mi> </Mrow> </Math> Heusler Compound*, Phys. Rev. B **93**, 094417 (2016).

[14] K. Elphick, W. Frost, M. Samiepour, T. Kubota, K. Takanashi, H. Sukegawa, S. Mitani, and A. Hirohata, *Heusler Alloys for Spintronic Devices: Review on Recent Development and Future Perspectives*, Sci. Technol. Adv. Mater. **22**, 235 (2021).

[15] K. Hamaya and M. Yamada, *Semiconductor Spintronics with Co2-Heusler Compounds*, MRS Bull. **47**, 584 (2022).

[16] Y. Yoshida, T. Nakamichi, and M. Kawakami, *Magnetic Properties of a Ternary Alloy Mn0.5v0.5-YAly*, J. Phys. Soc. Japan **50**, 2203 (1981).

[17] T. Nakamichi and C. V. Stager, *Phenomenological Formula of NMR Satellite of Heusler Alloys and Magnetic Structure of Mn2VAl*, J. Magn. Magn. Mater. **31**–**34**, 85 (1983).

[18] R. Weht and W. Pickett, *Half-Metallic Ferrimagnetism in (Formula Presented)*, Phys. Rev. B - Condens. Matter Mater. Phys. **60**, 13006 (1999).

[19] C. Jiang, M. Venkatesan, and J. M. D. Coey, *Transport and Magnetic Properties of Mn2VAl: Search for Half-Metallicity*, Solid State Commun. **118**, 513 (2001).

[20] I. Galanakis, P. H. Dederichs, and N. Papanikolaou, *Slater-Pauling Behavior and Origin of the Half-Metallicity of the Full-Heusler Alloys*, Phys. Rev. B **66**, 174429 (2002).

[21] K. Ozdogan, I. Galanakis, E. Şaşioglu, and B. Aktaş, *Search for Half-Metallic Ferrimagnetism in V-Based Heusler Alloys Mn 2VZ (Z ≤ Al, Ga, In, Si, Ge, Sn)*, J. Phys. Condens. Matter **18**, 2905 (2006).

[22] T. Kubota, K. Kodama, T. Nakamura, Y. Sakuraba, M. Oogane, K. Takanashi, and Y. Ando, *Ferrimagnetism in Epitaxially Grown Mn2VAl Heusler Alloy Investigated by Means of Soft X-Ray Magnetic Circular Dichroism*, Appl. Phys. Lett. **95**, 222503 (2009).

[23] R. Y. Umetsu and T. Kanomata, *Spin Stiffness Constant of Half-Metallic Ferrimagnet in Mn-Based Heusler Alloys*, Phys. Procedia **75**, 890 (2015).

[24] K. Fukuda, M. Oogane, and Y. Ando, *Structural and Magnetic Properties in Mn2VAl Full-Heusler Epitaxial Thin Films*, IEEE Trans. Magn. **53**, 2600304 (2017).

[25] S. Yamada, K. Kudo, R. Sadakari, and K. Hamaya, *Epitaxial Mn2VAl Films with L21 - Ordered Structure for All-Heusler Stacks*, J. Magn. Magn. Mater. **561**, 169644 (2022).

[26] C. Klewe, M. Meinert, J. Schmalhorst, and G. Reiss, *Negative Spin Polarization of Mn2VGa Probed by Tunnel Magnetoresistance*, J. Phys. Condens. Matter **25**, 76001 (2013).

[27] H. Suto, V. Barwal, K. Simalaotao, Z. Li, K. Masuda, T. Sasaki, Y. Miura, and Y. Sakuraba, *Negative Spin Polarization of Mn2VGa Heusler Alloy Thin Films Studied in Current-Perpendicular-to-Plane Giant Magnetoresistance Devices*, J. Appl. Phys. **135**, 203901 (2024).

[28] Z. H. Li et al., *Enhancing Atomic Ordering, Magnetic and Transport Properties of Mn2VGa Heusler Alloy Thin Films toward Negatively Spin-Polarized Charge Injection*, Acta Mater. **276**, 120110 (2024).

[29] H. Kurt, K. Rode, P. Stamenov, M. Venkatesan, Y.-C. Lau, E. Fonda, and J. M. D. Coey, *Cubic <math Display="inline"> <mrow> <msub> <mrow> <mi>Mn</Mi> </Mrow> <mrow> <mn>2</Mn> </Mrow> </Msub> <mi>Ga</Mi> </Mrow> </Math> Thin Films: Crossing the Spin Gap with Ruthenium*, Phys. Rev. Lett. **112**, 027201 (2014).

[30] T. Kubota et al., *Magnetoelastic Anisotropy in Heusler-Type <math> <msub> <mi Mathvariant="normal">Mn</Mi> <mrow> <mn>2</Mn> <mo>−</Mo> <mi>δ</Mi> </Mrow> </Msub> <msub> <mi Mathvariant="normal">CoGa</Mi> <mrow> <mn>1</Mn> <mo>+</Mo> <mi>δ</Mi> </Mrow> </Msub> </Math> Film*, Phys. Rev. Mater. **6**, 044405 (2022).

[31] C. Banerjee, N. Teichert, K. E. Siewierska, Z. Gercsi, G. Y. P. Atcheson, P. Stamenov, K. Rode, J. M. D. Coey, and J. Besbas, *Single Pulse All-Optical Toggle Switching of Magnetization without Gadolinium in the Ferrimagnet Mn2RuxGa*, Nat. Commun. **11**, 4444 (2020).

[32] P. D. Bentley et al., *Cubic-Type Heusler Compound <math> <mrow> <msub> <mi>Mn</Mi> <mn>2</Mn> </Msub> <mi>FeGa</Mi> </Mrow> </Math> Thin Film with Strain-Induced Large Perpendicular Magnetic Anisotropy*, Phys. Rev. Mater. **7**, 064404 (2023).

[33] J.-G. Zhu, X. Zhu, and Y. Tang, *Microwave Assisted Magnetic Recording*, IEEE Trans. Magn. **44**, 125 (2008).

[34] S. Bosu, H. Sepehri-Amin, Y. Sakuraba, S. Kasai, M. Hayashi, and K. Hono, *High Frequency Out-of-Plane Oscillation with Large Cone Angle in Mag-Flip Spin Torque Oscillators for Microwave Assisted Magnetic Recording*, Appl. Phys. Lett. **110**, 142403 (2017).

[35] W. Zhou, H. Sepehri-Amin, T. Taniguchi, S. Tamaru, Y. Sakuraba, S. Kasai, H. Kubota, and K. Hono, *Inducing Out-of-Plane Precession of Magnetization for Microwave-*

Assisted Magnetic Recording with an Oscillating Polarizer in a Spin-Torque Oscillator, Appl. Phys. Lett. **114**, 172403 (2019).

[36] N. Asam, H. Suto, S. Tamaru, H. Sepehri-Amin, A. Bolyachkin, T. Nakatani, W. Zhou, H. Kubota, and Y. Sakuraba, *Analysis Method of a Spin-Torque Oscillator Using Dc Resistance Change during Injection Locking to an External Microwave Magnetic Field*, Appl. Phys. Lett. **119**, 142405 (2021).

[37] M. Takagishi, N. Narita, H. Iwasaki, H. Suto, T. Maeda, and A. Takeo, *Design Concept of MAS Effect Dominant MAMR Head and Numerical Study*, IEEE Trans. Magn. **57**, 3300106 (2021).

[38] Y. Nakagawa, M. Takagishi, N. Narita, A. Takeo, and T. Maeda, *Multiple Spin Injection Into Coupled Field Generation Layers for Low Current Operation of MAMR Heads*, IEEE Trans. Magn. **58**, 3201005 (2022).

[39] C. Bellouard, H. Rapp, B. George, S. Mangin, G. Marchal, and J. Ousset, *Negative Spin-Valve Effect i/A Trilayers*, Phys. Rev. B - Condens. Matter Mater. Phys. **53**, 5082 (1996).

[40] C. Vouille, A. Barthélémy, F. E. Mpondo, A. Fert, P. A. Schroeder, S. Y. Hsu, A. Reilly, and R. Loloee, *Microscopic Mechanisms of Giant Magnetoresistance*, Phys. Rev. B - Condens. Matter Mater. Phys. **60**, 6710 (1999).

[41] M. AlHajDarwish, H. Kurt, S. Urazhdin, A. Fert, R. Loloee, W. P. Pratt, and J. Bass, *Controlled Normal and Inverse Current-Induced Magnetization Switching and Magnetoresistance in Magnetic Nanopillars*, Phys. Rev. Lett. **93**, 157203 (2004).

[42] X. Li, H. Li, M. Jamali, and J.-P. Wang, *Damping Constant Measurement and Inverse Giant Magnetoresistance in Spintronic Devices with Fe4N*, AIP Adv. **7**, 125303 (2017).

[43] H. Suto, T. Nakatani, Y. Kota, A. Nagarjuna, H. Iwasaki, K. Amemiya, T. Mitsui, S. Sakai, S. Li, and Y. Sakuraba, *Study on FeCr Thin Film for a Spintronic Material with Negative Spin Polarization*, J. Magn. Magn. Mater. **557**, 169474 (2022).

[44] H. Suto, T. Nakatani, N. Asam, H. Iwasaki, and Y. Sakuraba, *Evaluation of Spin-Transfer-Torque Efficiency Using Magnetization Reversal against a Magnetic Field: Comparison of FeCr with Negative Spin Polarization and NiFe*, Appl. Phys. Express **16**, 013003 (2023).

[45] K. Sunaga, M. Tsunoda, K. Komagaki, Y. Uehara, and M. Takahashi, *Inverse Tunnel Magnetoresistance in Magnetic Tunnel Junctions with an Fe4N Electrode*, J. Appl. Phys. **102**, 013917 (2007).

[46] S. Yasui, S. Honda, J. Okabayashi, T. Yanase, T. Shimada, and T. Nagahama, *Large Inverse Tunnel Magnetoresistance in Magnetic Tunnel Junctions with an <math Display="inline" Overflow="scroll"> <msub> <mi>Fe</Mi> <mn>3</Mn> </Msub> <msub> <mrow> <mrow> <mi Mathvariant="normal">O</Mi> </Mrow> </Mrow> <mn>4</Mn> </Msub> </Math> Ele*, Phys. Rev. Appl. **15**, 034042 (2021).

[47] J. Korringa, *On the Calculation of the Energy of a Bloch Wave in a Metal*, Physica **13**, 392 (1947).

[48] W. Kohn and N. Rostoker, *Solution of the Schrödinger Equation in Periodic Lattices with an Application to Metallic Lithium*, Phys. Rev. **94**, 1111 (1954).

[49] *Akai-KKR (Machikaneyama) Http://Kkr.Issp.u-Tokyo.Ac.Jp*.

[50] J. P. Perdew, K. Burke, and M. Ernzerhof, *Generalized Gradient Approximation Made Simple*, Phys. Rev. Lett. **77**, 3865 (1996).

[51] G. Kresse and J. Furthmüller, *Efficient Iterative Schemes for Ab Initio Total-Energy Calculations Using a Plane-Wave Basis Set*, Phys. Rev. B **54**, 11169 (1996).

[52] C. G. Van De Walle and J. Neugebauer, *First-Principles Calculations for Defects and Impurities: Applications to III-Nitrides*, J. Appl. Phys. **95**, 3851 (2004).

[53] B. Hülsen, M. Scheffler, and P. Kratzer, *Thermodynamics of the Heusler Alloy <math Display="inline"> <mrow> <msub> <mrow> <mtext>Co</Mtext> </Mrow> <mrow> <mn>2</Mn> <mo>−</Mo> <mi>x</Mi> </Mrow> </Msub> <msub>*

718 *<mrow> <mtext>Mn</Mtext> </Mrow> <mrow> <mn>1</Mn> <mo>+</Mo>*
719 *<mi>x</Mi> </Mrow> </Ms*, Phys. Rev. B **79**, 094407 (2009).
720 [54] P. E. Blöchl, *Projector Augmented-Wave Method*, Phys. Rev. B **50**, 17953 (1994).
721 [55] G. Kresse and D. Joubert, *From Ultrasoft Pseudopotentials to the Projector Augmented-*
722 *Wave Method*, Phys. Rev. B **59**, 1758 (1999).
723 [56] R. Landauer, *Electrical Resistance of Disordered One-Dimensional Lattices*, Philos.
724 Mag. **21**, 863 (1970).
725 [57] P. Giannozzi et al., *QUANTUM ESPRESSO: A Modular and Open-Source Software*
726 *Project for Quantum Simulations of Materials*, J. Phys. Condens. Matter **21**, 395502
727 (2009).
728 [58] P. Giannozzi et al., *Advanced Capabilities for Materials Modelling with Quantum*
729 *ESPRESSO*, J. Phys. Condens. Matter **29**, 465901 (2017).
730 [59] P. J. Webster, *Magnetic and Chemical Order in Heusler Alloys Containing Cobalt and*
731 *Manganese*, J. Phys. Chem. Solids **32**, 1221 (1971).
732 [60] Y. Takamura, R. Nakane, and S. Sugahara, *Analysis of L 21 -Ordering in Full-Heusler*
733 *Co2 FeSi Alloy Thin Films Formed by Rapid Thermal Annealing*, J. Appl. Phys. **105**,
734 07B109 (2009).
735 [61] O. Sakata et al., *Beamline for Surface and Interface Structures at SPring-8*, Surf. Rev.
736 Lett. **10**, 543 (2003).
737 [62] H. Tajiri, H. Yamazaki, H. Ohashi, S. Goto, O. Sakata, and T. Ishikawa, *A Middle*
738 *Energy-Bandwidth x-Ray Monochromator for High-Flux Synchrotron Diffraction:*
739 *Revisiting Asymmetrically Cut Silicon Crystals*, J. Synchrotron Radiat. **26**, 750 (2019).
740 [63] G. Li et al., *Effect of Nonstoichiometry on the Half-Metallic Character of Co <math>*
741 *<msub> <mrow/> <mn>2</Mn> </Msub> </Math> MnSi Investigated through*
742 *Saturation Magnetization and Tunneling Magnetoresistance Ratio*, Phys. Rev. B **89**,
743 014428 (2014).

[64] *See Supplemental Material at [URL Will Be Inserted by Publisher] for FMR Measurements and Anisotropic MR Measurements of the Single-Layer MVA Samples.*, (n.d.).

[65] J. W. Jung, Z. Jin, Y. Shiokawa, and M. Sahashi, *Investigations of Interface Spin Asymmetry and Interfacial Resistance in Fe x Co100 − x /Ag Interface*, J. Appl. Phys. **117**, 17A323 (2015).

[66] V. Barwal, H. Suto, and Y. Sakuraba, *Reducing Critical Current for Spin-Transfer-Torque-Induced Magnetization Reversal in CPP-GMR Devices: The Effect of Low Damping and Interfacial Spin Scattering Asymmetry of Co2FeGa0.5Ge0.5 Heusler Alloy*, Prep. (n.d.).

[67] J. Barnaś, A. Fert, M. Gmitra, I. Weymann, and V. K. Dugaev, *From Giant Magnetoresistance to Current-Induced Switching by Spin Transfer*, Phys. Rev. B - Condens. Matter Mater. Phys. **72**, 024426 (2005).

Fig. 1 (one column)

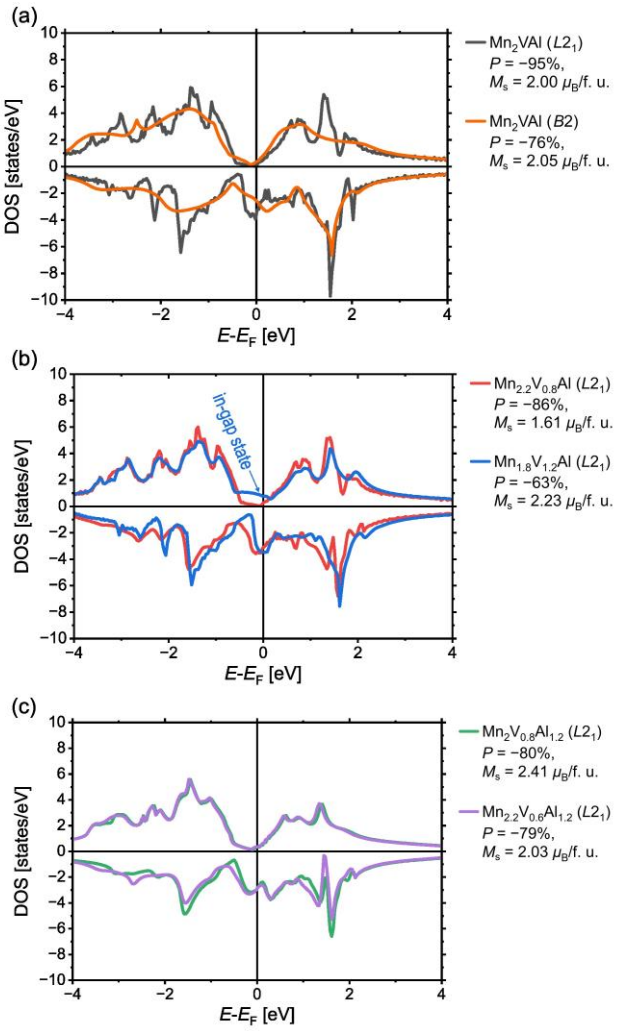

Fig. 1. First-principles calculations of the spin-dependent total DOSs for (a) $L2_1$- and $B2$-ordered Mn_2VAl, (b) $L2_1$-ordered $Mn_{2.2}V_{0.8}Al$ and $Mn_{1.8}V_{1.2}Al$, and (c) $L2_1$-ordered $Mn_2V_{0.8}Al_{1.2}$ and $Mn_{2.2}V_{0.6}Al_{1.2}$. Spin polarization (P) at E_F and M_s are also shown.

Fig. 2 (one column)

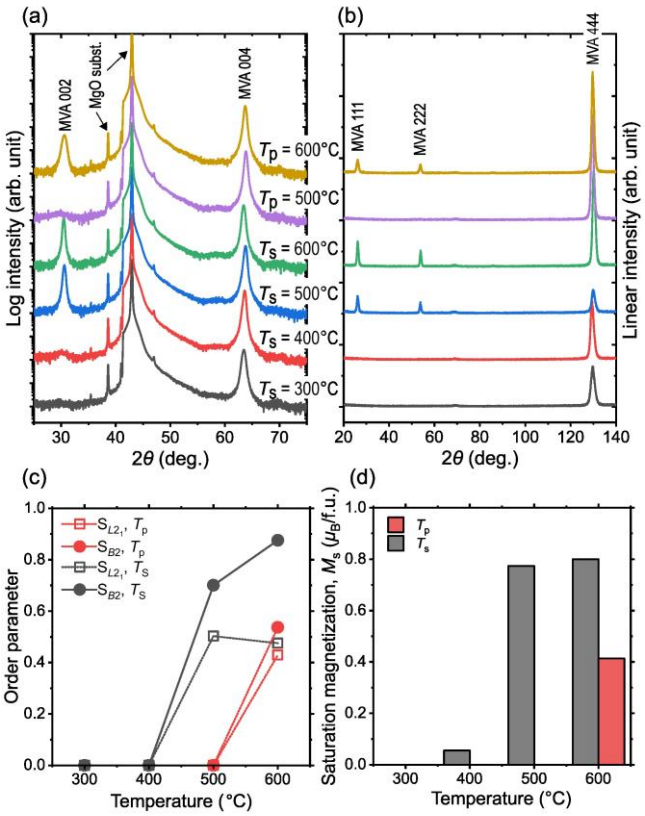

Fig. 2. (a) Out-of-plane and (b) [111]-direction XRD profiles for type-A Mn_2VAl samples (T_s = 300ºC–600ºC and T_p = 500ºC–600ºC). The marked temperature above each line is the same for (a) and (b), and data are offset for clarity. (c) Temperature dependence of S_{B2} and S_{L2_1} are calculated from peak intensities in (a) and (b). (d) Process temperature dependence of M_s.

Fig. 3 (one column)

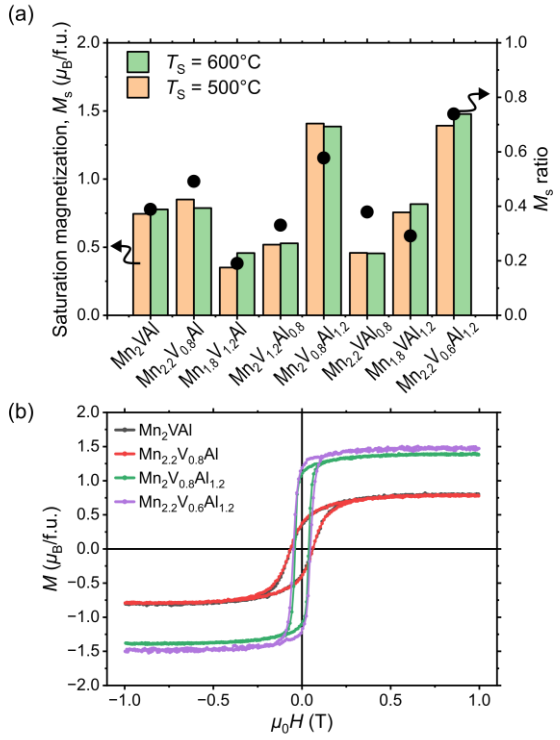

Fig. 3. (a) Composition dependence of M_s obtained for type-A samples (T_s = 500ºC and 600ºC), and black circles represent M_s ratio for T_s = 600ºC. (b) *M*–*H* curves for type-A samples (T_s = 600ºC) of Mn_2VAl, $Mn_{2.2}V_{0.8}Al$, $Mn_2V_{0.8}Al_{1.2}$, and $Mn_{2.2}V_{0.6}Al_{1.2}$.

Fig. 4 (one column)

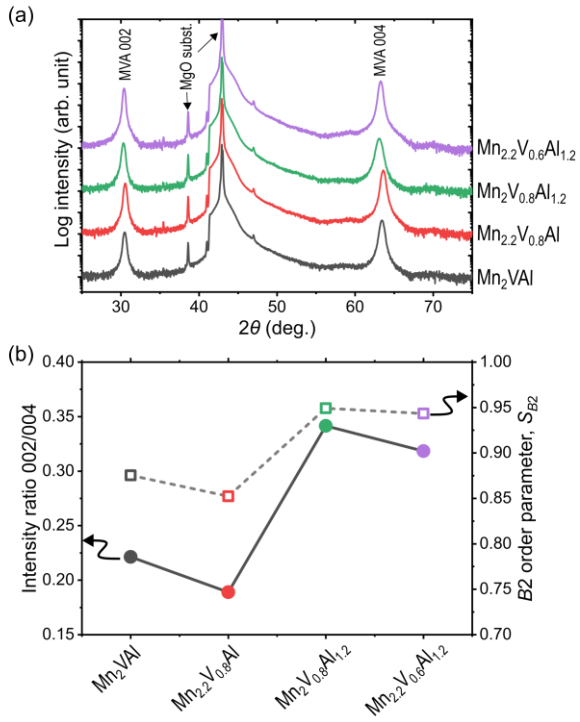

Fig. 4. (a) Out-of-plane and (b) [111]-direction XRD profiles for type-A samples (T_s = 600ºC) of Mn_2VAl, $Mn_{2.2}V_{0.8}Al$, $Mn_2V_{0.8}Al_{1.2}$, and $Mn_{2.2}V_{0.6}Al_{1.2}$. Data are offset for clarity. (b) Composition dependence of the intensity ratio of the 002 peak over the 004 peak and corresponding S_{B2}.

Fig. 5 (one column)

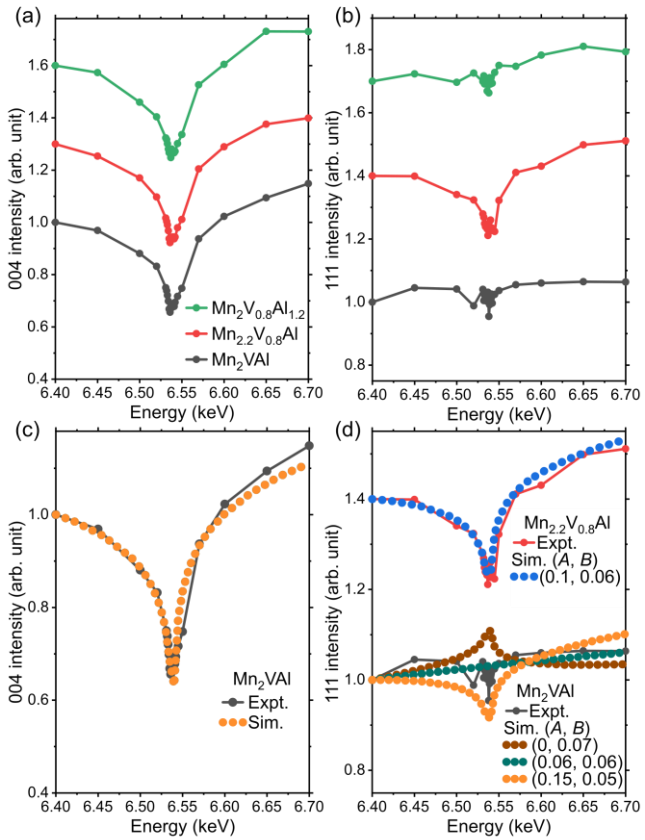

Fig. 5. X-ray energy dependence of the experimentally yielded intensities of (a) 004 and (b) 111 reflections around the Mn *K*-absorption edge obtained for type-A samples (T_s = 600ºC) of Mn_2VAl, $Mn_{2.2}V_{0.8}Al$, and $Mn_2V_{0.8}Al_{1.2}$. Curves were normalized by the intensity at 6.4 keV and offset for clarity. Legends are common for (a) and (b). Corresponding simulations of (c) 004 and (d) 111 reflections. Simulated profiles for various Mn–V (*A*) and Mn–Al (*B*) disorders are overlaid on the experimental results.

Fig. 6 (one column)

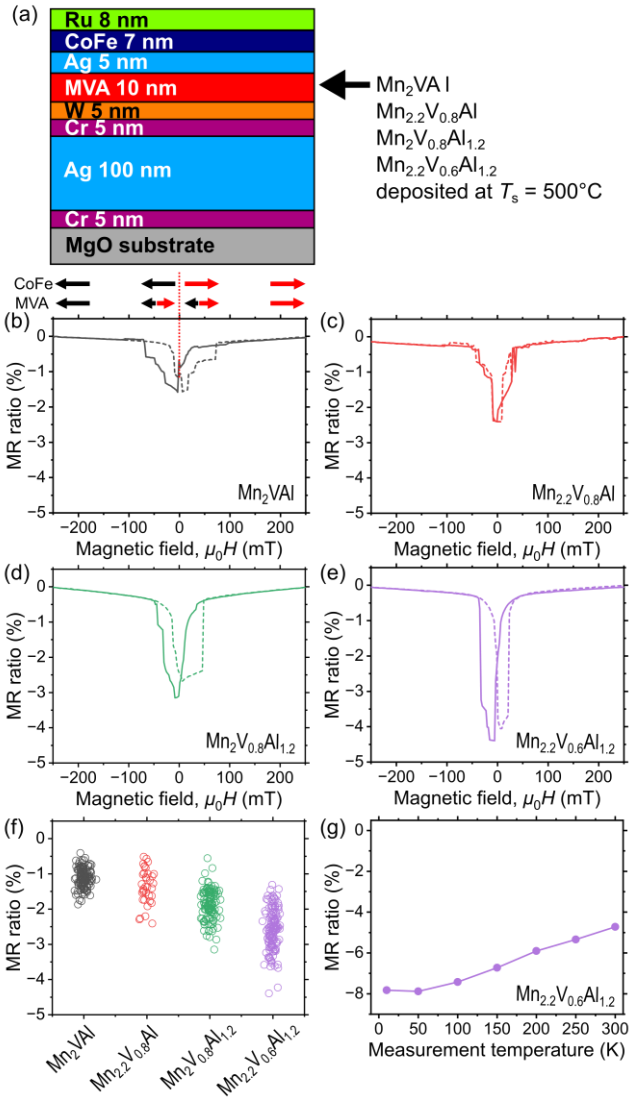

Fig. 6. (a) Structure of type-B samples used to fabricate CPP-GMR devices. (b)–(e) Examples of *R*–*H* curves measured for CPP-GMR devices comprising Mn_2VAl, $Mn_{2.2}V_{0.8}Al$, $Mn_2V_{0.8}Al_{1.2}$, and $Mn_{2.2}V_{0.6}Al_{1.2}$. Solid and dashed lines represent the downward and upward *H* sweeps, respectively. (b) Schematics depicting the magnetization configurations of the MVA and CoFe layers for the downward *H* sweep. (e) Composition dependence of the MR ratio distribution. (g) MR ratio as a function of measurement temperature for the $Mn_{2.2}V_{0.6}Al_{1.2}$ sample.

803 **Fig. 7 (one column)**

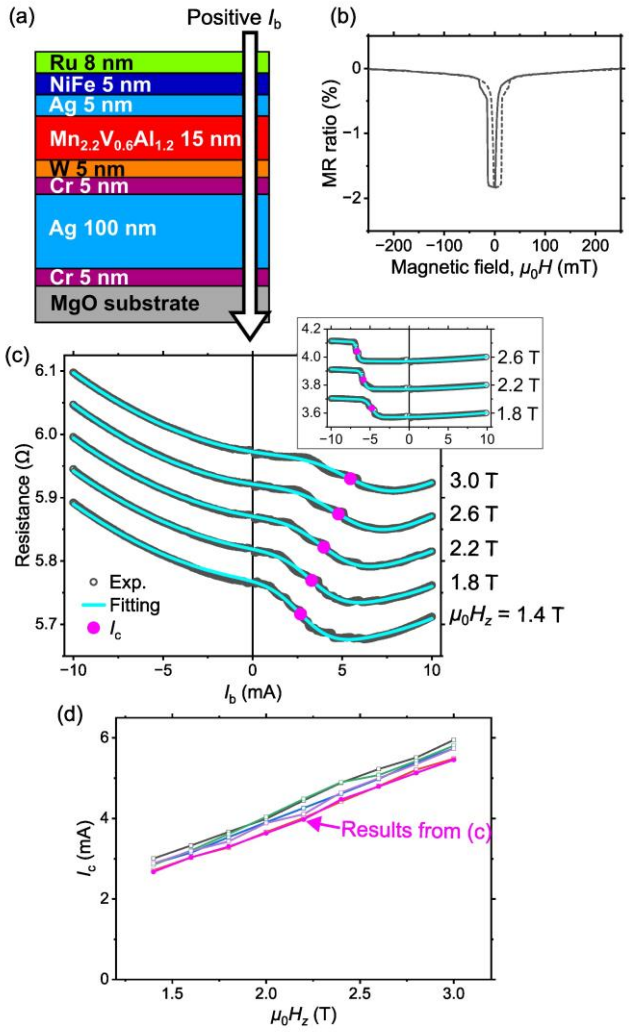

804

805 **Fig. 7.** (a) Structure of the type-C samples. Arrow indicates the positive current direction. (b)
806 Example of *R*–*H* curve. Solid and dashed lines represent the downward and upward *H* sweeps,
807 respectively. (c) *R*–I_b curves and H_z values together with fitting curves and I_c. Data are offset for
808 clarity. Inset shows reference results for an identical set of measurements conducted on a CPP-
809 GMR with CFGG instead of MVA, which are from [66]. (d) I_c–H_z curves from the results from
810 (c) and I_c–H_z curves from several other devices from the same sample.

811

Fig. 8 (two column)

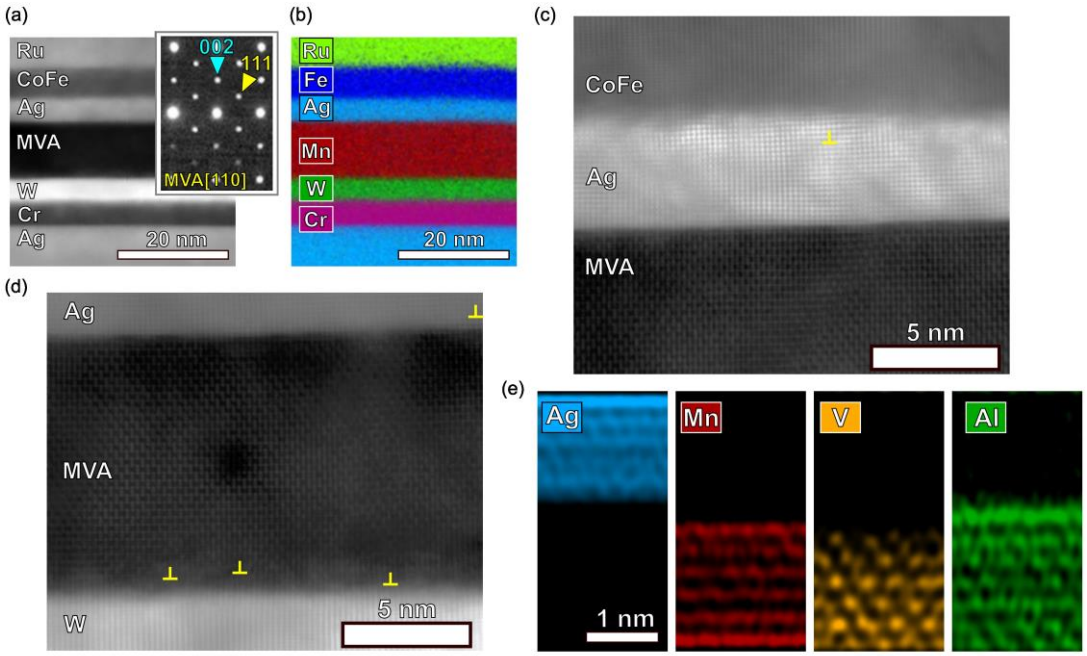

Fig. 8. (a) HAADF-STEM image of the type-B sample with a $Mn_{2.2}V_{0.6}Al_{1.2}$ layer. The inset shows NBED patterns obtained for the MVA layer. (b) Corresponding EDS mapping. Only the Fe (Mn) signal from the CoFe (MVA) layer is shown for simplicity. (c) and (d) magnified HAADF-STEM image at the MVA/Ag/CoFe and W/MVA/Ag regions, respectively. Yellow ⊥ symbols indicate atomic dislocations. (e) Atomic-resolution EDS mapping at the MVA/Ag interface.

820 **Fig. 9 (two column)**

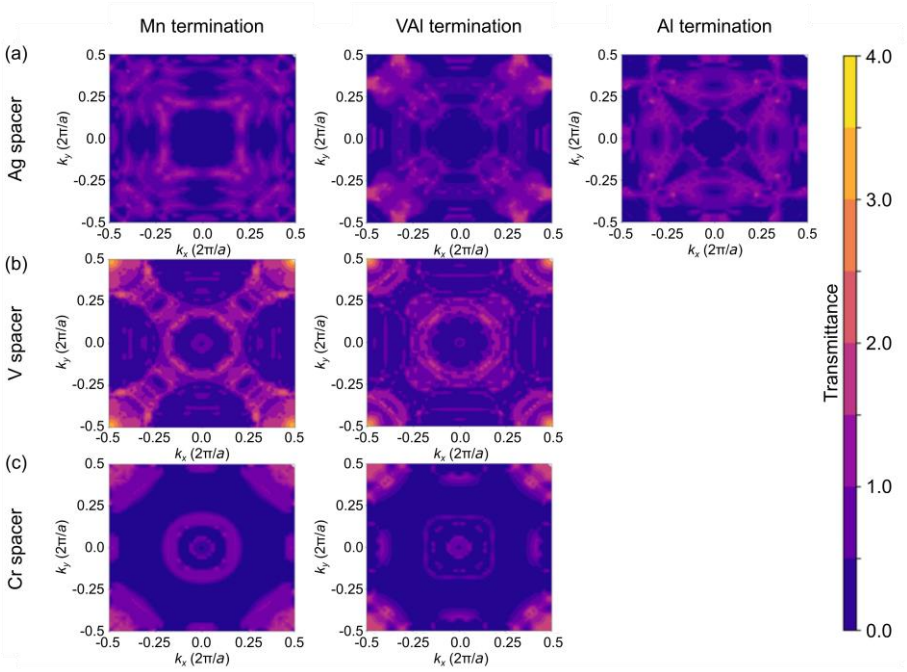

821

822 **Fig. 9.** In-plane wave vector dependence of minority-spin transmittance in the parallel
823 magnetization configuration calculated for (a) $Mn_2VAl/Ag/Mn_2VAl$ (001) with Mn, VAl, and Al
824 terminations, (b) $Mn_2VAl/V/Mn_2VAl$(001) with Mn and VAl terminations, and (c)
825 $Mn_2VAl/Cr/Mn_2VAl$(001) with Mn and VAl terminations

826

Supplemental Material

Negative spin polarization and effect of composition on the atomic order and electronic structure of Mn_2VAl Heusler alloy thin films

Hirofumi Suto[1], Vineet Barwal[1], Keisuke Masuda[1], Kodchakorn Simalaotao[1], Taisuke Sasaki[1], Yoshio Miura[1], Hiroo. Tajiri[2], Loku Singgappulige Rosantha Kumara[2], Tomoyuki. Koganezawa[2],and Yuya Sakuraba[1]

[1]Research Center for Magnetic and Spintronic Materials, National Institute for Materials Science (NIMS), Tsukuba, 305-0047, Japan

[2]Japan Synchrotron Radiation Research Institute (JASRI), Kouto, 679-5198, Japan

Ferromagnetic resonance (FMR) measurement of the single layer MVA sample for $Mn_{2.2}V_{0.6}Al_{1.2}$

Figures S1(a) and S1(b) show the frequency dependence of the FMR resonance field and half-width of the FMR peaks measured for the type-A sample (T_s = 600°C) for $Mn_{2.2}V_{0.6}Al_{1.2}$, respectively. The FMR measurements were conducted by applying a in-plane magnetic field (H). From the slope of the halfwidth, the damping parameter of $Mn_{2.2}V_{0.6}Al_{1.2}$ was estimated to be 0.025.

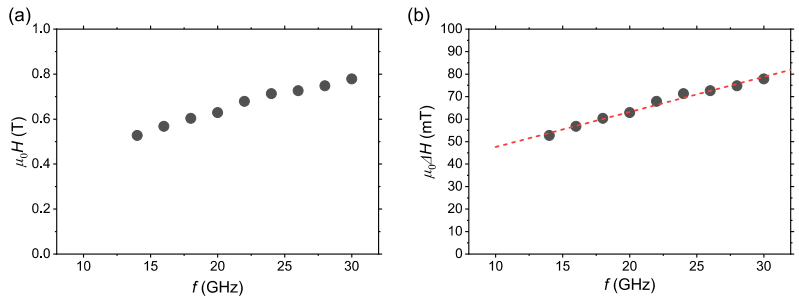

FIG. S1. (a) Resonance field of FMR versus frequency for the type-A sample (T_s = 600°C) for $Mn_{2.2}V_{0.6}Al_{1.2}$. (b) Corresponding half-width of the FMR peaks versus frequency.

Anisotropic magnetoresistance measurements of the single layer MVA samples

Figures S.2(a)-(d) shows the anisotropic magnetoresistance (AMR) ratio as a function of ϕ for type-A samples (T_s = 600ºC) of Mn_2VAl, $Mn_{2.2}V_{0.8}Al$, $Mn_2V_{0.8}Al_{1.2}$, and $Mn_{2.2}V_{0.6}Al_{1.2}$. The current was applied along MVA [110] and MVA [100] and the measurement temperature was set from 10 to 300 K. All the MVA samples exhibit positive AMR ratios for the current along the MVA [110] direction, and negative ratios as the current direction aligned with the MVA [100] direction. Such sign reversal of the AMR ratio by the current direction was reported in Mn_2VGa and explained from the viewpoint of DOS [1]. The similarity in the AMR measurement between MVA and Mn_2VGa is consistent with the fact that these materials have similar DOS. The AMR results changed with the compositions as follows. The results for Mn_2Val and $Mn_{2.2}V_{0.8}Al$ are similar, showing small temperature dependence. In $Mn_2V_{0.8}Al_{1.2}$, the AMR results for the current along [110] shows gradual decrease with lowering the temperature. In $Mn_{2.2}V_{0.6}Al_{1.2}$, the AMR results for both [110] and [100] current directions decrease with lowering the temperature. The amplitude of negative AMR for the [100] current direction was enhanced in comparison with the other compositions. These changes imply the modification in the electronic band structure.

Further analysis is necessary to understand the origin of the composition dependence, which is beyond the scope of this study.

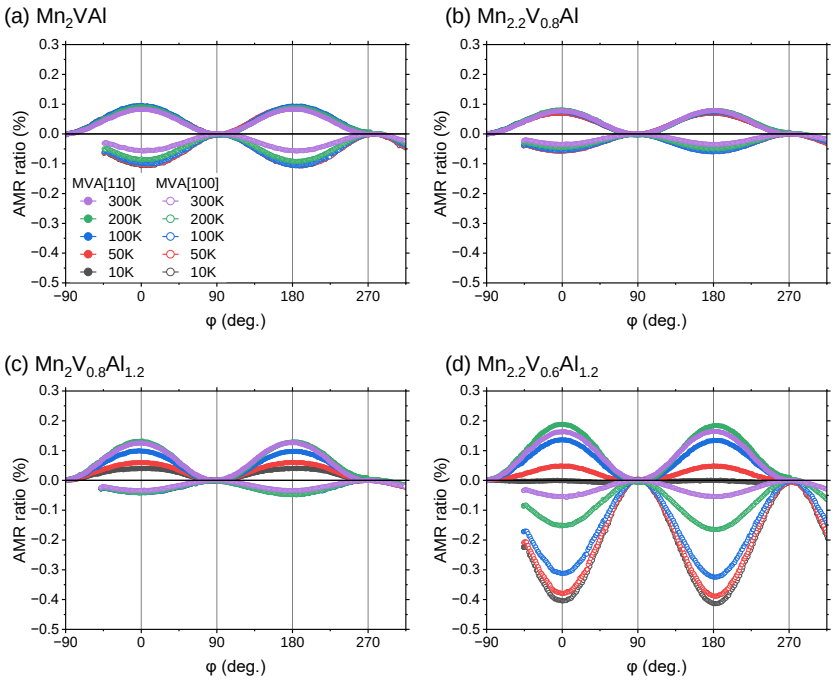

FIG. S2. Angle dependence of the AMR ratio of or the type-A sample (T_s = 600°C) for (a) Mn_2VAl, (b) $Mn_{2.2}V_{0.8}Al$, (c) $Mn_2V_{0.8}Al_{1.2}$, and (d) $Mn_{2.2}V_{0.6}Al_{1.2}$ measured from 10 to 300 K. The current was applied along the MVA [110] and MVA [100] directions. The legends are common in (a)-(d).

Reference

[1] Z.H. Li, H. Suto, V. Barwal, K. Masuda, T.T. Sasaki, Z.X. Chen, H. Tajiri, L.S.R. Kumara, T. Koganezawa, K. Amemiya, S. Kokado, K. Hono, and Y. Sakuraba, "*Enhancing atomic ordering, magnetic and transport properties of Mn_2VGa Heusler alloy thin films toward negatively spin-polarized charge injection*," Acta Mater. **276**, 120110 (2024).